scientific reports

Check for updates

OPEN

Highly improved supercapacitance properties of $MnFe_2O_4$ nanoparticles by MoS_2 nanosheets

Samira Sharifi, Kourosh Rahimi & Ahmad Yazdani✉

Manganese ferrite ($MnFe_2O_4$) nanoparticles were synthesized via a hydrothermal method and combined with exfoliated MoS_2 nanosheets, and the nanocomposite was studied as a supercapacitor. X-ray diffractometry and Raman spectroscopy confirmed the crystalline structures and structural characteristics of the nanocomposite. Transmission electron microscopy images showed the uniform size distribution of $MnFe_2O_4$ nanoparticles (~ 13 nm) on few-layer MoS_2 nanosheets. UV–visible absorption photospectrometry indicated a decrease in the bandgap of $MnFe_2O_4$ by MoS_2, resulting in a higher conductivity that is suitable for capacitance. Electrochemical tests showed that the incorporation of MoS_2 nanosheets largely increased the specific capacitance of $MnFe_2O_4$ from 600 to 2093 F/g (with the corresponding energy density and power density of 46.51 Wh/kg and 213.64 W/kg, respectively) at 1 A/g, and led to better charge–discharge cycling stability. We also demonstrated a real-world application of the $MnFe_2O_4/MoS_2$ nanocomposite in a two-cell asymmetric supercapacitor setup. A density functional theory study was also performed on the $MnFe_2O_4/MoS_2$ interface to analyze how a MoS_2 monolayer can enhance the electronic properties of $MnFe_2O_4$ towards a higher specific capacitance.

There have been increasing demands in the past few decades for superior energy storage and conversion devices to address the basic energy-related needs of the ever-growing population in the world[1]. Therefore, it is indispensable to develop energy-storage devices with high energy capacities, long lifetimes, and high cycling stability to overcome the impending exhaustion of fossil fuel reserves and alleviate environmental concerns[2]. Supercapacitors are among the most-promising energy-storage devices owing to their longer lifespan than secondary batteries and their higher capacitance and reliability than conventional dielectric capacitors[2]. There are two classifications for supercapacitors based on their energy storage mechanisms: (1) electrochemical double-layer capacitors that accumulate charges at their electrode/electrolyte interface and (2) pseudocapacitors that handle charges via fast and reversible redox reactions on electrochemically active sites[3]. However, it is yet challenging to design and develop electrode materials to realize these anticipated features and efficiently store/deliver energy[4–6].

There has been recently growing attention to two-dimensional (2D) layered materials for a variety of applications including energy production and storage, sensors, photocatalysts, etc.[7–9]. Recent developments suggest that 2D transition metal dichalcogenides (TMDs) such as MoS_2, $MoSe_2$, WS_2, TiS_2, NbS_2, and VS_2 have great potential to fill the gap between the current performance and the modern requirements of energy-storage devices as electrodes of electrochemical supercapacitors[10–13]. In general, TMDs make use of fast and reversible faradaic redox reactions (also known as pseudocapacitance) that involve ions and electrons in their charge storage mechanism[14,15]. In particular, few-layer MoS_2 nanosheets have been found promising because of their large surface area, which acts as a substrate to hold other nanoparticles, and high thermal stability[16].

Among various transition metals[17], nickel, manganese, and cobalt are promising in the field of supercapacitors due to their high electrochemical activity and low cost as well as the abundance of their oxide/hydroxide compounds[18–24]. It has also been demonstrated that the spinel ferrites of these metals (MFe_2O_4, M is a transition metal) deliver much better electrochemical performance due to their richer valence electron, different redox states, synergistic effects between their metal ions, electrochemical stability, and chemical and mechanical stability, suitable for batteries and supercapacitors[14,25–29]. Recently, we have compared the supercapacitance of $MnFe_2O_4$, $CoFe_2O_4$, and $NiFe_2O_4$ nanoparticles, and found that $MnFe_2O_4$ exhibits better supercapacitance properties[14,15].

It is thus interesting to make composites of $MnFe_2O_4$ nanoparticles and few-layer MoS_2 nanosheets, as a 2D TMD, to utilize their synergistic effects to achieve improved electronic properties[30,31]. In such a composite, the

Condensed Matter Physics Group, Department of Basic Sciences, Tarbiat Modares University, Jalal-Ale-Ahmad Avenue, Tehran, Iran. ✉email: yazdania@modares.ac.ir

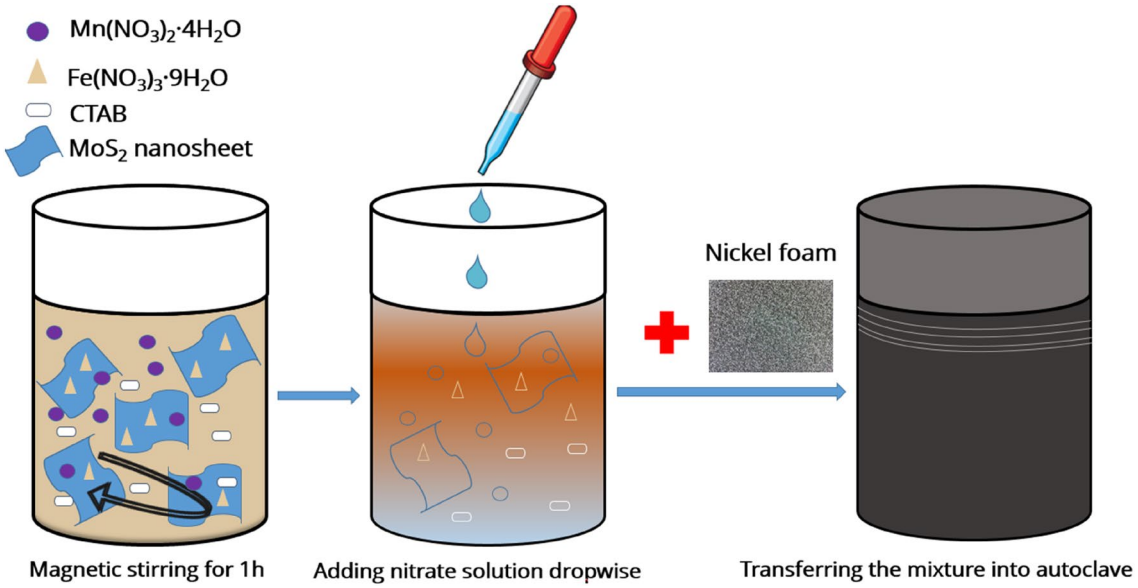

Figure 1. The procedure to synthesize the $MnFe_2O_4/MoS_2$-coated Ni foam (drawn using Microsoft PowerPoint 2016, downloadable from www.microsoft.com).

$MnFe_2O_4$ nanoparticles would prevent the MoS_2 nanosheets from restacking, and in a similar manner, the MoS_2 nanosheets would act as a substrate on which the $MnFe_2O_4$ nanoparticles can be uniformly distributed so that they would not be agglomerated. The mutual effect would result ultimately in a larger active surface area that can promote electrolyte access and provide more channels for migration of ions and electrons[32].

To the best of our knowledge, there is not yet any report on supercapacitance properties of the composite of MoS_2 nanosheets (as a TMD) decorated with $MnFe_2O_4$ (as a metal ferrite) nanoparticles, and it is thus interesting to see how the probable synergistic effect of them can be useful to achieve improved electrochemical energy storage performance. Here, we reported the successful fabrication of the $MnFe_2O_4/MoS_2$ nanocomposite on nickel foam via a facile hydrothermal method and tested the nanocomposite as a supercapacitor electrode.

Experimental

Manganese(II) nitrate tetrahydrate ($Mn(NO_3)_2.4H_2O$), iron(III) nitrate nonahydrate ($Fe(NO_3)_3.9H_2O$), cetyltrimethylammonium bromide (CTAB), N-Methyl-2-pyrrolidone (NMP), acetonitrile, polyvinylidene difluoride (PVDF), activated carbon (AC), and hydrogen peroxide (H_2O_2) were purchased from Merck Co. (> 98%) and bulk molybdenum disulfide (MoS_2, 99%) powder was purchased from Sigma-Aldrich Co, and the precursors were used without any further purification.

Synthesis. Few-layer MoS_2 nanosheets were exfoliated from bulk MoS_2 powder in mixed solvents based on the work of Lu et al.[33]. First, 20 mg MoS_2 powder was mixed in 0.5 ml acetonitrile and it was ground for 1 h. The obtained powder was mixed in a solution of 30 wt% H_2O_2 and NMP (H_2O_2:NMP volume ratio = 1:19), and it was stirred for 10 h at 35 °C to be exfoliated. The mixture was dried in a furnace for 5 h at 300 °C to evaporate NMP. To in-situ synthesize the $MnFe_2O_4/MoS_2$ nanocomposite on a Ni foam substrate using a hydrothermal method, 0.1 g of the obtained MoS_2 nanosheets was first dispersed into 40 ml deionized water, and 0.4 g $Fe(NO_3)_3.9H_2O$, 0.125 g $Mn(NO_3)_2.4H_2O$, and 0.125 g CTAB were dissolved into the dispersion by stirring for 2 h. Next, 1 ml of 25% ammonia solution was added into the prepared mixture under vigorous stirring until its pH reached ~ 9. The obtained mixture was transferred into a Teflon-lined autoclave and a nickel foam substrate, cut in the size of 1×2 cm^2, and cleaned with deionized water, acetone, and ethanol, was put into it. The autoclave was subsequently heated in an oven at 180 °C for 15 h, and then it was allowed to cool to room temperature in ambient air. Finally, the $MnFe_2O_4/MoS_2$-coated nickel foam was washed several times with deionized water and ethanol and dried in an oven at 80 °C for 2 h. For comparative purposes, $MnFe_2O_4$-coated nickel foam was also synthesized via a similar method without adding MoS_2. The prepared substrates were used for further characterizations. Figure 1 shows a schematic of various steps followed in our synthesis procedure.

Characterization. Crystalline structures of the samples were identified using a PANalytical X'pert MPD (Philips) diffractometer with a Cu-Kα radiation source (λ = 0.15406 nm). Structural fingerprints of the ferrites and the MoS_2 nanosheets were investigated by a Takram P50C0R10 Raman spectrometer (Teksan Co., Iran) employing an Nd:YAG laser (λ_{ex} = 532 nm) at room temperature. To observe structural shapes ph of the prepared nanostructure, field-emission scanning electron microscopy (FESEM) and transmission electron microscopy (TEM) images were taken by MIRA3TESCAN-XMU and PHILIPS CM30 NETHERLANDS instruments, respectively. The elemental compositions of the samples were analyzed by energy-dispersive X-ray spectroscopy (EDS) mapping using a BRUKER XFlash 6 I10 instrument. The topographical information of MoS_2 nanosheets

was acquired by atomic force microscopy (AFM, Veeco Autoprobe CP-research). The optical properties of the nanocomposites were examined using a Unico 4802 UV–Vis photospectrometer.

Electrochemical tests. The supercapacitive performance of the samples was investigated using a three-electrode setup containing the coated Ni foam substrate (1 cm^2) as the working electrode, a square-shaped platinum sheet (1 cm^2, 99.99%) as the counter electrode, and Ag/AgCl as the reference electrode in a 3 M KOH solution at room temperature. Although Ni foam shows a battery-like behavior[34], we chose it because of its large specific surface area that can accommodate more parts of active materials. In this regard, the calculated specific capacitance is better not to be compared with other literature. Nevertheless, we aim at comparing the specific capacitances of our samples with each other to find how the incorporation of MoS_2 nanosheets can enhance the specific capacitance of $MnFe_2O_4$ nanoparticles. The electrochemical measurements involved cyclic voltammetry (CV), galvanostatic charging/discharging (GCD), and electrochemical impedance spectroscopy (EIS) techniques using a VSP-300 Multichannel Potentiostat/Galvanostat/EIS instrument (Bio-Logic Science Instruments). The CV measurements were recorded at different scan rates (5–100 mV/s) within the potential window of 0–0.55 V. The GCD measurements were recorded at different current densities with the potential window of 0–0.4 V.

Asymmetric two-electrode supercapacitor setup. An asymmetric two-electrode supercapacitor device was assembled by using activated carbon (AC) as the negative electrode and the $MnFe_2O_4/MoS_2$ nanocomposite as the positive electrode. The electrodes were separated by a filter paper wetted with 3 M KOH solution as the electrolyte. The AC electrode was prepared from the activated carbon and PVDF, as a binder, with the weight ratio of 95:5 dispersed in NMP. The prepared dispersion was coated on a nickel foam substrate by a brush and the obtained electrode was dried in an oven at 60 °C for 10 h. The masses of the positive and negative electrodes were balanced according to the following equation[14]:

$$\frac{m_+}{m_-} = \frac{C_S^- \Delta V^-}{C_s^+ \Delta V^+} \tag{1}$$

where m is the mass, C_s is the specific capacitance, ΔV is the potential window, and (+) and (−) denote the positive and the negative electrodes, respectively. The coated mass on the negative electrode was ~ 3 mg. The CV measurements were recorded at different scan rates (5–100 mV/s) within the potential window of 0–1.5 V. The GCD measurements were recorded at different current densities with the potential window of 0–1.5 V.

Computational methods. First-principles calculations were performed in the framework of density functional theory (DFT), as implemented in the Quantum Espresso package (version 6.3)[35], using the plane-wave basis set and ultrasoft pseudopotentials[36]. The spin polarization was included in both geometry optimizations and electronic structure calculations. The generalized gradient approximation (GGA) developed by Perdew, Burke, and Ernzerhof (PBE)[37] was applied for electron exchange–correlation functionals with the on-site Coulomb repulsion U terms[38] of U(Mn) = 3.9 eV and U(Fe) = 5.3 eV to reproduce experimental data[14]. The kinetic energy cutoffs for wavefunctions and charge densities were set to 50 and 450 Ry, respectively. To sample the first Brillouin zone for electronic structure calculations, we adopted the k-point grid of 9 × 9 × 1 for the unit cell of the MoS_2 monolayer, 6 × 6 × 5 for the bulk $MnFe_2O_4$, and the k-point grid of 6 × 6 × 1 for the $MnFe_2O_4/MoS_2$ interface. All structures were fully relaxed until the convergence criteria of energy and force became less than 10^{-6} Ry and 10^{-3} Ry/Bohr, respectively. All crystal images were produced by VESTA (version 3.4.5)[39].

Results and discussions

The XRD patterns of the samples are shown in Fig. 2. The XRD pattern of the bulk MoS_2 shows all the characteristic peaks corresponding to the hexagonal phase of MoS_2 with the JCPDS card No. 00-037-1492. However, the XRD pattern of the exfoliated MoS_2 nanosheets shows only the weak (002) diffraction peak, indicating the successful exfoliation of MoS_2 into few-layer nanosheets. In the pattern of $MnFe_2O_4$ nanoparticles, the peaks at 2θ = 18°, 30°, 35°, 43°, 53°, 57°, and 63° correspond to (111), (220), (311), (400), (422), (511), and (440), which are attributed to the cubic spinel structure of $MnFe_2O_4$ with the space group of *Fd* 3 *m* with the JCPDS card No. 96-591-0064[32]. No other peak is seen, indicating the purity of the prepared nanoparticles. To calculate the crystallite size and the lattice strain for the $MnFe_2O_4$ nanoparticles, the Williamson-Hall analysis formula was applied[40]

$$\beta_{hkl} cos\theta_{hkl} = \frac{k\lambda}{D} + 4\varepsilon sin\theta_{hkl} \tag{2}$$

where θ_{hkl} is the diffraction peak angle, β_{hkl} is the full-width at half maximum of the (hkl) diffraction peak, D is the crystallite size, K is the shape factor approximated to 0.9, λ is the incident X-ray wavelength (1.5406 Å), and ε is the lattice strain[41]. Accordingly, D and ε are calculated from the Y-intercept and the slope of the line fitted on the plot of 4sinθ versus βCosθ, respectively[32,41]. Therefore, the crystallite size of the $MnFe_2O_4$ nanoparticles was calculated ~ 9.5 nm with a compressive strain of − 0.0144. In the XRD pattern of the $MnFe_2O_4/MoS_2$-coated Ni foam, all of the peaks related to $MnFe_2O_4$ are seen with a peak at 2θ = 14° related to few-layer MoS_2 nanosheets and two other peaks at 2θ = 43° and 53° corresponding to the Ni foam substrate. This indicates that the nanocomposite has been successfully prepared, with no other impurities.

Figure 3 shows the Raman spectra of the samples. The Raman spectrum of few-layer MoS_2 nanosheets (Fig. 3A) show two peaks at 385 and 407 cm^{-1} attributed to the in-plane (E_{2g}) and the out-of-plane (A_{1g}) vibration modes, respectively, of few-layer MoS_2[32]. In the Raman spectrum of the bulk MoS_2 powder, the

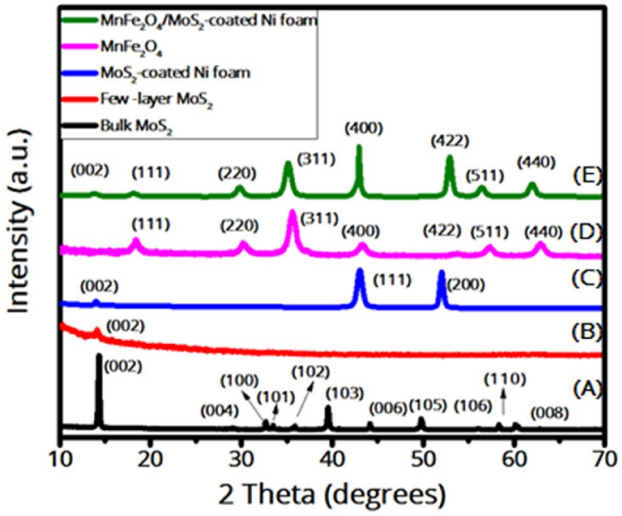

Figure 2. XRD patterns of (**A**) bulk MoS_2, (**B**) exfoliated MoS_2 nanosheets, (**C**) MoS_2-coated Ni foam, (**D**) $MnFe_2O_4$ nanoparticles, and (**E**) $MnFe_2O_4$/MoS_2-coated Ni foam.

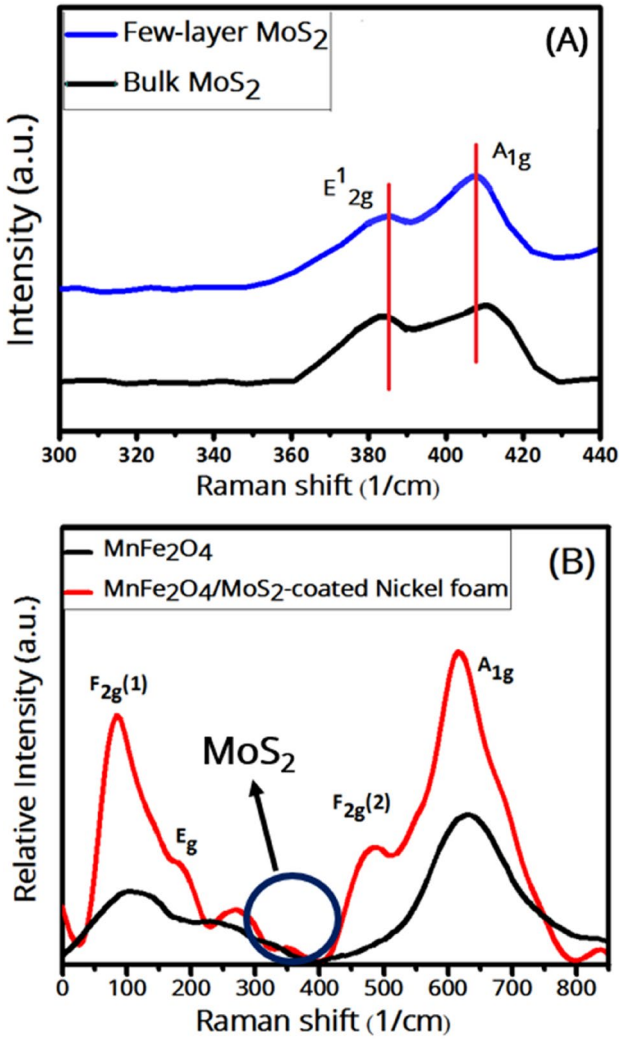

Figure 3. Raman spectra of (**A**) $MnFe_2O_4$ nanoparticles, and $MnFe_2O_4$/MoS_2-coated Ni foam, (**B**) few-layer MoS_2 nanosheets.

lower-wavenumber mode shifts slightly towards a lower wavenumber (387 cm^{-1}), and the higher-wavenumber mode shifts slightly towards a higher wavenumber (411 cm^{-1}). The shifts are consistent with layer-dependent Raman modes of MoS_2 sheets[42], confirming that our exfoliated MoS_2 nanosheets are few-layer. In the Raman spectrum of $MnFe_2O_4$ nanoparticles (Fig. 3B), the E_g band (189 cm^{-1}) is due to the asymmetric and symmetric bending of O with respect to Fe, the $F_{2g}(1)$ band (107 cm^{-1}) is due to the translational movement of the whole tetrahedron (FeO_4), and the A_{1g} band (630 cm^{-1}) is due to the symmetric stretching of oxygen atoms along Fe–O (or Mn–O) tetrahedral bonds[14]. The bands confirm the inverse spinel structure of the $MnFe_2O_4$[43]. The Raman spectrum of the $MnFe_2O_4/MoS_2$ nanocomposite coated on a nickel foam shows the peaks due to $MnFe_2O_4$ and also the $F_{2g}(2)$ band, which is due to the asymmetric stretching of Fe/Mn–O bonds, as well as the E_2g band of few-layer MoS_2 nanosheets, confirming the presence of both $MnFe_2O_4$ and MoS_2 in the nanocomposite. Here, the peaks due to $MnFe_2O_4$ have shifted toward lower wavenumbers as compared to the pure ferrite nanoparticles (617, 484, 195, and 86 cm^{-1} corresponding to A_{1g}, $F_{2g}(1)$, E_g, and $F_{2g}(2)$ modes, respectively), which can be due to the applied strain when they are composited with MoS_2 nanosheets. On the other hand, no Raman mode is expected from the nickel foam, as all metals with one atom per unit cell, like Ni, are Raman inactive[44].

UV–vis absorption spectroscopy is a powerful tool to investigate the optical properties of semiconductor materials[45]. UV–Vis absorption spectra of the samples with their corresponding Tauc plots are shown in Fig. 4. Optical bandgaps of the samples were estimated using the classical Tauc relation.

$$(\alpha h\nu)^n = B\left(h\nu - E_g\right) \tag{3}$$

where α, ν, n, B, h, and E_g is the absorption coefficient, the photon frequency, a constant that depends on the bandgap type (1/2 and 2 for direct and indirect band gaps), a constant, the Planck's constant, and the optical bandgap, respectively. The optical band gap is estimated from an extrapolation of the linear part of $(\alpha h\nu)^2$ versus the photon energy (hν) for direct bandgaps. The UV–Vis spectrum of MoS_2 nanosheets shows four characteristic peaks at 684, 625, 481, and 399 nm, corresponding to four different electronic transitions denoted with A, B, C, and D, consistent with previously reported values[33]. The few-layer MoS_2 nanosheets exhibit a bandgap of 1.7 eV, consistent with the literature[33]. The $MnFe_2O_4$ sample shows a bandgap of 1.6 eV[14]. It is observed that the bandgap of the $MnFe_2O_4/MoS_2$ nanocomposite is almost smaller than that of the pure $MnFe_2O_4$ nanoparticles. This is due to the creation of intermediate states between the valence band and the conduction band of $MnFe_2O_4$ resulting from MoS_2. The lower bandgap of the $MnFe_2O_4/MoS_2$ nanocomposite as compared to the pure $MnFe_2O_4$ nanoparticles and the presence of intermediate states can increase the conductivity of the nanocomposite which in turn can enhance its capacitance.

FESEM images of the prepared samples are shown in Fig. 5. The pure MoS_2 nanosheets in Fig. 5A,B are sufficiently wide with a lateral size of about 2 to 3 μm, which is appropriate as a substrate to hold other nanoparticles. Some obvious foldings can be seen in these MoS_2 nanosheets, and one can conclude that they are few-layer. Figure 5C shows an AFM micrograph of an exfoliated MoS_2 nanosheets on a mica substrate. According to the height profile of the shown dashed line drawn, the thickness of the sheet is ~ 5 nm, indicating that the exfoliated MoS_2 nanosheets are few-layer. Figure 5D shows that the $MnFe_2O_4$ nanoparticles are highly uniform in size with an average diameter of ~ 10 nm, which is very close to the size calculated from the XRD spectrum (~ 9.5 nm).

The elemental composition and distribution of different atoms in the prepared $MnFe_2O_4/MoS_2$ nanocomposite ($MnFe_2O_4$ nanoparticles attached on MoS_2 nanosheets) were also analyzed by energy-dispersive X-ray spectroscopy (EDS) mapping, shown in Fig. 6. It is seen that Mo and S atoms are uniformly distributed on the entire mapped window, indicating the presence of MoS_2 nanosheets. Furthermore, the distribution of Mn, Fe, and O atoms are almost uniform and similar, with some aggregates of them in the lower-left part of the mapped window. This uniform and dense distribution of the ferrite nanoparticles enabled by the presence of MoS_2 nanosheets can provide a larger surface to volume ratio, required for an enhanced charge transfer and, in turn, a higher capacitance.

Figure 7 shows TEM images of the few-layer MoS_2 nanosheets, the $MnFe_2O_4$ nanoparticles, and the $MnFe_2O_4/MoS_2$ nanocomposite. Figure 7A shows a few-layer MoS_2 nanosheet with some wrinkles, indicating its low thickness. The $MnFe_2O_4$ nanoparticles in Fig. 7B are nearly uniform in diameter, with a mean diameter of ~ 13 nm, which is very close to the sizes found from XRD calculations and FESEM measurements. Figure 7C shows the $MnFe_2O_4/MoS_2$ nanocomposite, where both MoS_2 nanosheets and $MnFe_2O_4$ nanoparticles can be seen.

Figure 8 shows the CV curves of the samples at various scan rates, where two peaks are seen with positive and negative currents corresponding to oxidation and reduction processes at the electrode's surface, respectively[46]. As it is seen, by increasing the scan rate the oxidation and reduction peaks shift to higher and lower potentials, respectively, because a shorter time would be available for the electrolyte ions to access the electrode's surface. However, there is a trade-off between potential and time. Besides, at higher scan rates, both the area under the CV curve and the current increase. Nevertheless, it is seen that the area enclosed in a CV curve (or equivalently, the specific capacitance) decreases as the scan rate increases. This is because at higher scan rates, due to the fast migration of ions, some parts of the active surface areas become inaccessible for the charge storage process[14,18,47]. Figure 8 also represents the galvanostatic charge/discharge (GCD) curves of the samples at different current densities in a potential window of 0 to 0.4 V. It is seen that the discharge time of the samples decreases as the current density increases, explained above. The specific capacitance of the electrodes was calculated from their discharge curves according to the equation[14,18]:

$$C_{sp} = 2I\frac{\int V dt}{m(\Delta V)^2} \tag{4}$$

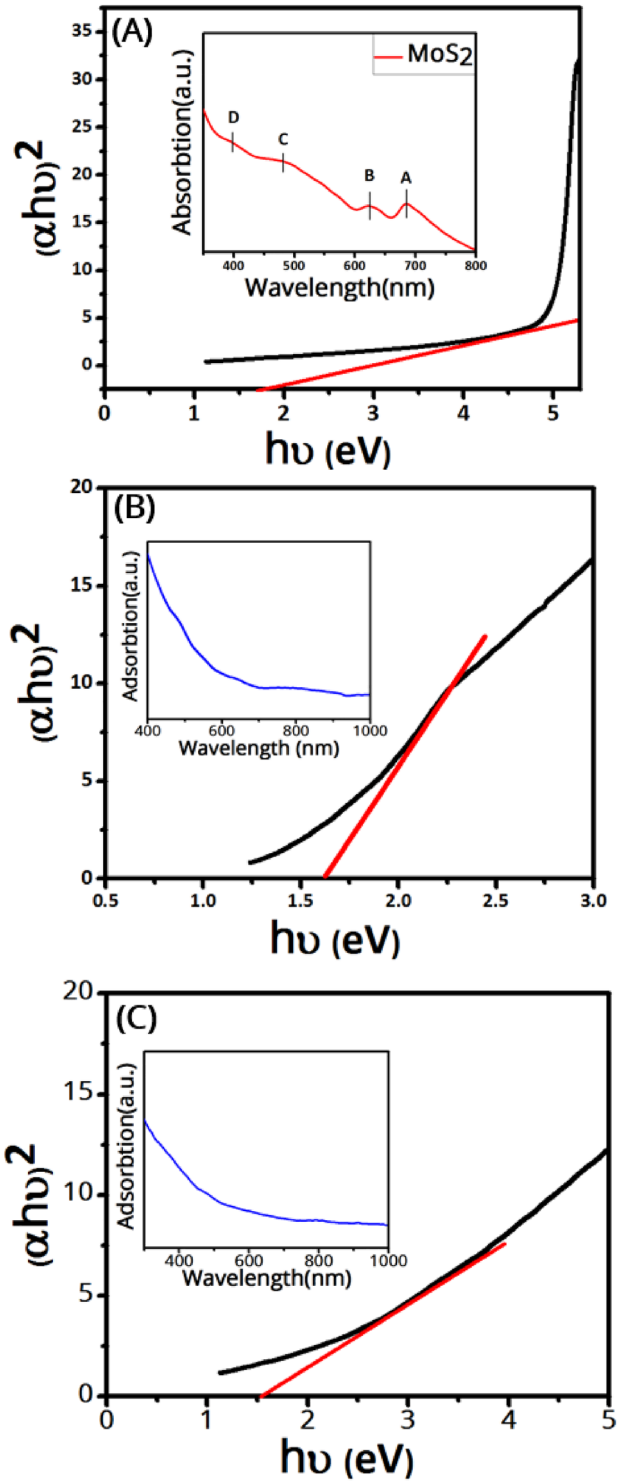

Figure 4. UV–Vis absorption spectra and Tauc plots (insets) of (**A**) MoS_2 nanosheets, (**B**) $MnFe_2O_4$ nanoparticles, and (**C**) the $MnFe_2O_4/MoS_2$ nanocomposite.

at different current densities, where C_{sp}, I/m, $\int Vdt$, and ΔV are the specific capacitance (F/g), the current density (A/g), the area under the discharge curve, and the active potential window, respectively. It should be noted that for battery-type materials, where they have a plateau during their charging and discharging, the capacity should not be calculated using Eq. (4)[34]. However, in our GCD curves, there is no plateau, and instead, an oblique part is seen, consistent with a mostly-pseudocapacitive behavior. Such behavior is more observable in our two-electrode cell measurements (in Fig. 10). Therefore, it is safe to use the formula to calculate the specific capacitance values. The specific capacitances of the samples are reported in Table 1.

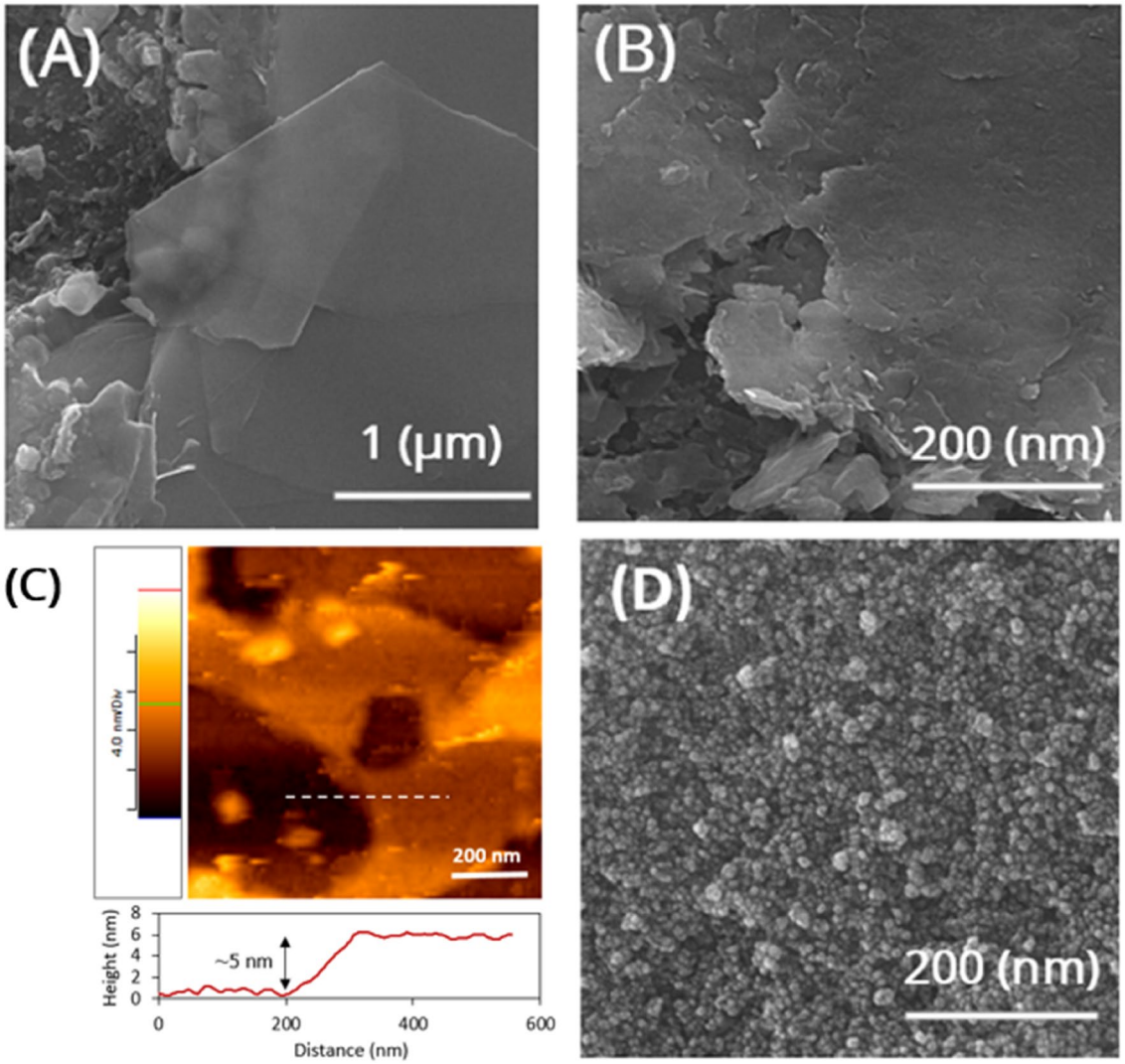

Figure 5. (**A**,**B**) FESEM and (**C**) AFM images of exfoliated few-layer MoS_2 nanosheets. (**D**) A FESEM image of the $MnFe_2O_4$ nanoparticles.

As it is seen in Fig. 9A, which compares the GCD curves of the samples at the current density of 1 A/g, the discharge time, or equivalently the specific capacitance, of the $MnFe_2O_4/MoS_2$ composite is more than those of both MoS_2 and $MnFe_2O_4$. This can be for several reasons. Firstly, MoS_2 is itself an active material for electrochemical reactions due to its electronic structure as well as layered structure, because it can accommodate electrolyte ions in its layered structure. Secondly, due to its versatile redox states, $MnFe_2O_4$ has a pseudocapacitive behavior. Therefore, both MoS_2 and $MnFe_2O_4$ contribute to the supercapacitance of the $MnFe_2O_4/MoS_2$ nanocomposite. On the other hand, MoS_2 nanosheets prevent the $MnFe_2O_4$ from agglomeration and aggregation. Similarly, $MnFe_2O_4$ nanoparticles prevent the MoS_2 nanosheets from restacking. This will increase the active surface area for charge storage processes. In the next section on DFT calculations, we will see how MoS_2 can redistribute the stored charges on $MnFe_2O_4$ to achieve an improved capacitance. As can be seen in Fig. 9B, the specific capacitance decreases as the current density increases, which is due to the ion diffusion mechanism. In other words, at a lower current density, the electrolyte ions have enough time to penetrate into the active sites on the electrode material, leading to a higher specific capacitance[14]. Figure 9C compares the CV curves of the prepared electrodes at the scan rate of 5 mV/s. The reduction and oxidation peaks are seen around 0.14 V and 0.4 V, respectively. As it is seen, the $MnFe_2O_4/MoS_2$ nanocomposite shows a larger CV-enclosed area than that of $MnFe_2O_4$, which is itself larger than that of MoS_2. This could indicate the higher capacitance of the $MnFe_2O_4/MoS_2$ nanocomposite than $MnFe_2O_4$. The incorporation of MoS_2 nanosheets largely increased the specific capacitance of $MnFe_2O_4$ from 600 to 2093 F/g at 1 A/g. The power densities of the MoS_2, $MnFe_2O_4$, and $MnFe_2O_4/MoS_2$ samples were obtained at the current density of 1 A/g, listed in Table 2, and their Ragone plots (energy density versus power density) are shown in Fig. 9D. The energy and power densities of the samples were calculated based on

$$E = \frac{1}{2} C_{sp} \Delta V^2 \tag{5}$$

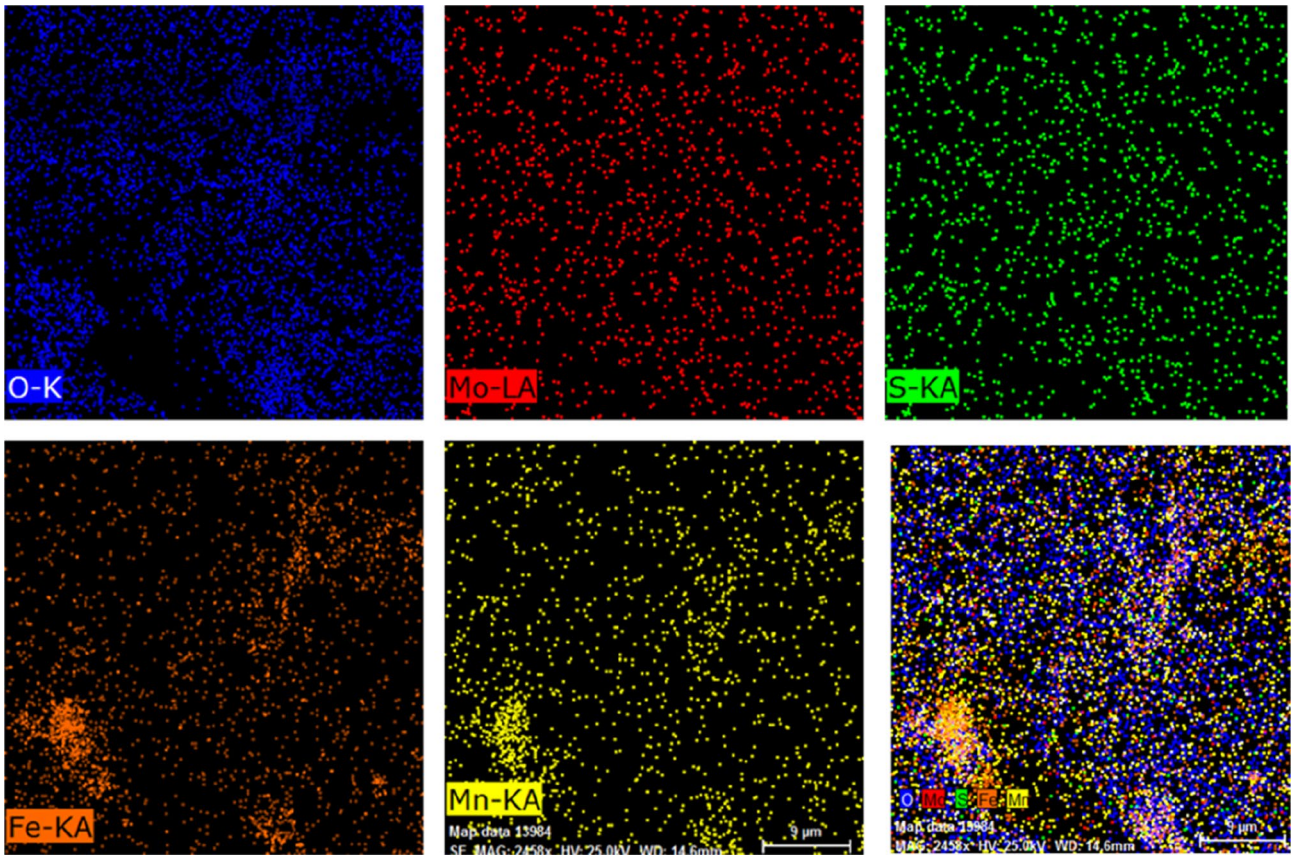

Figure 6. EDS mapping for different atoms in the $MnFe_2O_4/MoS_2$ nanocomposite.

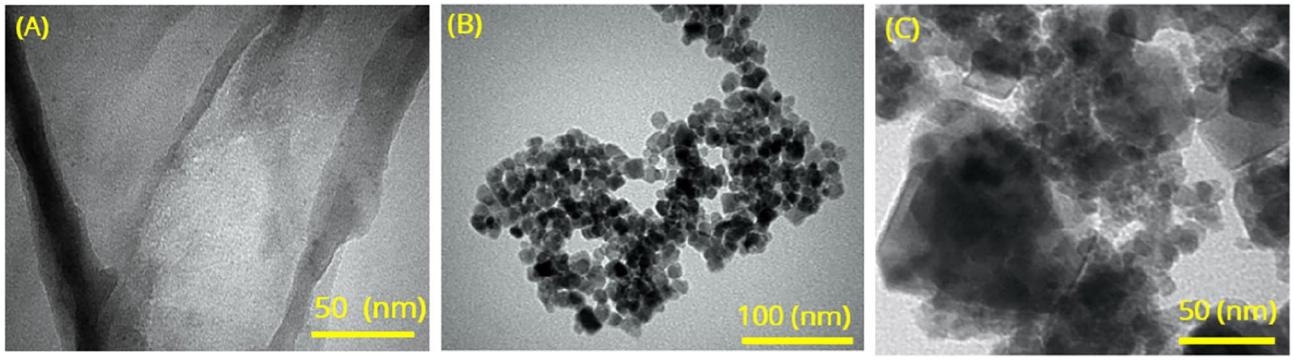

Figure 7. TEM images of (**A**) few-layer MoS_2 nanosheets, (**B**) $MnFe_2O_4$ nanoparticles, and (**C**) the $MnFe_2O_4/MoS_2$ nanocomposite.

$$P = \frac{E}{t} \tag{6}$$

respectively, where ΔV and t are the potential windows and the discharge time (h)[48]. Cyclic stability tests were performed at the current density of 20 A/g for 2000 GCD cycles, as shown in Fig. 9E. It is seen that the incorporation of MoS_2 nanosheets considerably improved the cycling stability of the pure $MnFe_2O_4$ nanoparticles. This can be due to the fact that MoS_2 prevents the $MnFe_2O_4$ nanoparticles from detaching from the electrode into the electrolyte, which can improve the capacitance stability of the composite. Electrochemical impedance spectroscopy (EIS) was used to analyze the resistance information of samples. The frequency range of the impedance measurements is 10 MHz–100 kHz. An EIS curve typically consists of two parts: (1) the high-frequency region is a semicircle and (2) the low-frequency region is a straight line, indicating the charge-transfer resistance, and an inclined line, indicating the diffusion of ions into the electrolyte[49,50]. According to the EIS plots in Fig. 9F, the charge transfer resistance of the samples is negligible. The internal resistance can be obtained from the slope of the curves intersecting the x-axis. According to the EIS plots, the internal resistance of the $MnFe_2O_4/$

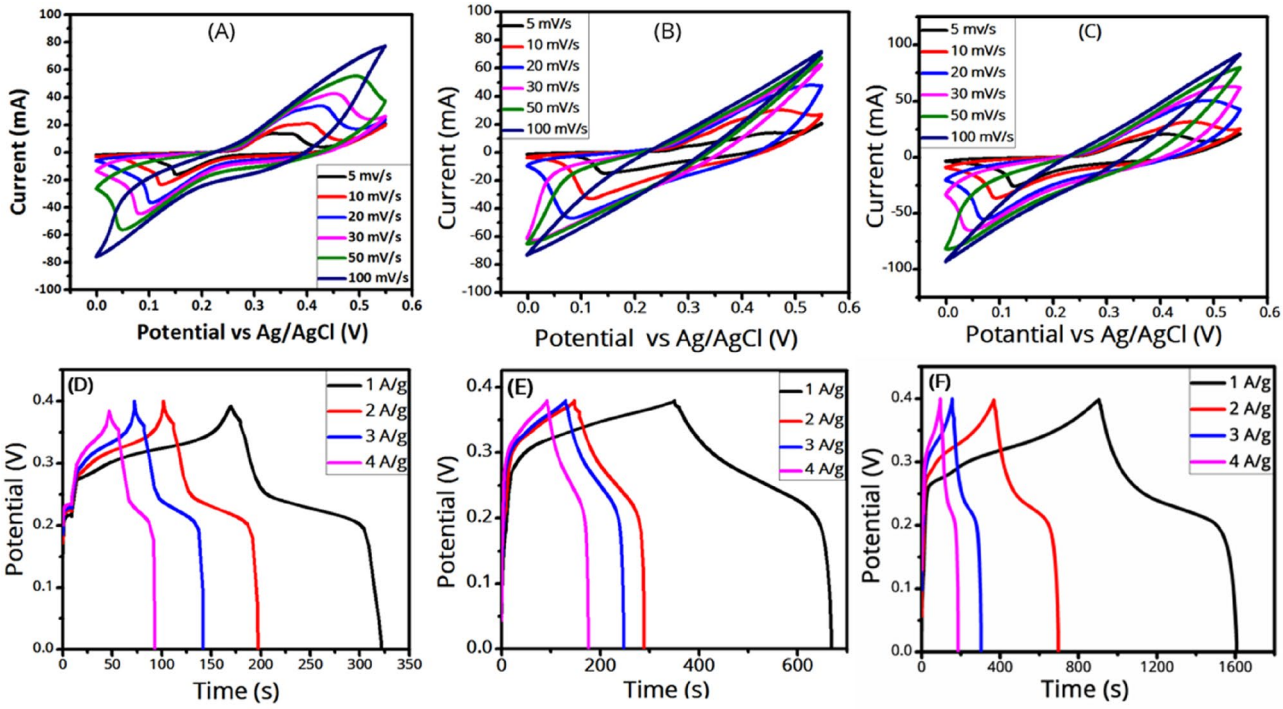

Figure 8. CV (at various scan rates) and GCD (at various current densities) curves of (**A**,**D**) few-layer MoS_2 nanosheets, (**B**,**E**) $MnFe_2O_4$ nanoparticles, and (**C**,**F**) the $MnFe_2O_4/MoS_2$ nanocomposite.

Current density (A/g)	Specific capacitance (F/g)		
	MoS_2 nanosheets	$MnFe_2O_4$	$MnFe_2O_4/MoS_2$
1	440	600	2093
2	428	520	1982
3	415	453	1870
4	346	375	1810

Table 1. Specific capacitance values of the samples at various current densities.

MoS_2 nanocomposite is lower than those of MoS_2 and $MnFe_2O_4$ (also see the DFT section), so it has a higher conductivity suitable for supercapacitance. To sum up, the comparative results show that the $MnFe_2O_4/MoS_2$ nanocomposite exhibits better capacitive performance compared to both MoS_2 and $MnFe_2O_4$.

Next, we assembled the ($MnFe_2O_4/MoS_2$)//AC asymmetric supercapacitor in a two-electrode setup, as discussed in the "Experimental" section. Figure 10A shows the CV curves of the device for incremental voltages to confirm its operating potential. It is seen that the capacity increases as the potential window increases, indicating the ability of the device to perform faradaic processes at higher voltages. Figure 10B shows the CV curves of the device for various scan rates at the potential window of 0–1.5 V, showing quasi-rectangular shapes that illustrate the good electrochemical reversibility of the device. Figure 10C shows the GCD curves of the device for various current densities. The charge and discharge parts of the GCD curves are almost symmetric, which demonstrates a small internal resistance drop, indicating the contributions from both the faradaic processes and the double layer capacitance[51]. Figure 10D illustrates the lighting up of a green light-emitting diode (LED) using the ($MnFe_2O_4/MoS_2$)//AC asymmetric supercapacitor.

DFT study

MoS_2 is a layered transition metal dichalcogenide where its layers are bound together by weak van der Waals (vdW) forces. Each MoS_2 monolayer consists of three atomic layers in the sequence of S-Mo-S. Bulk MoS_2 is a p-type indirect-bandgap semiconductor (1.23 eV), and its bandgap slightly increases to 1.8 eV as the number of layers decreases to one[52,53]. Figure 11A shows top and side views of the optimized structure of the MoS_2 monolayer and its atom-projected density of states. We found the optimized lattice constant of 3.18 Å and the Mo-S bond length of 2.41 Å, and the MoS_2 monolayer shows a direct bandgap of 1.76 eV at the K point, consistent with[53]. On the other hand, $MnFe_2O_4$ is an insulating, soft ferrimagnetic spinel ferrite, which crystallizes in a mixed-phase spinel structure[54] with an almost low inversion degree of 0.2, where 80% and 20% of Mn^{2+} ions

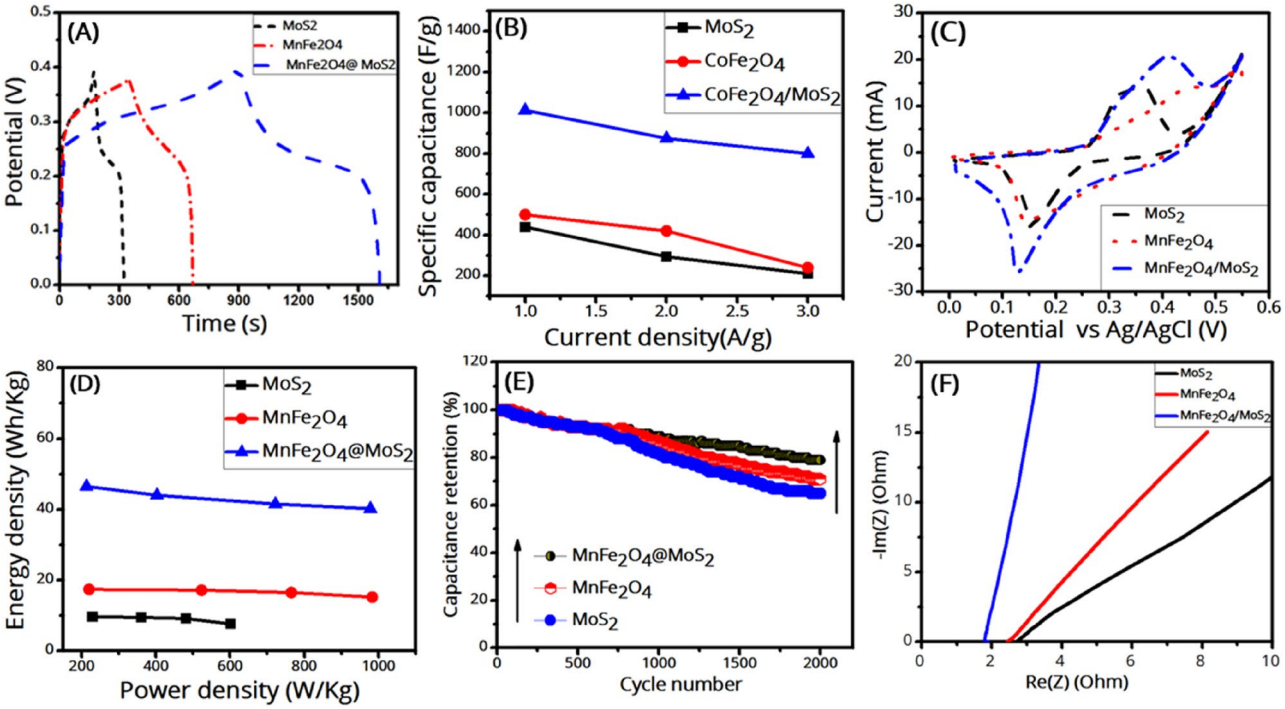

Figure 9. (**A**) GCD curves of the samples at the current density of 1 A/g, (**B**) specific capacitance versus current density for the samples, (**C**) CV curves of the samples at the scan rate of 5 mV/s, (**D**) Ragone plots (energy density versus power density) of the samples, (**E**) cycling stabilities of the samples during 2000 GCD cycles at the current density of 20 A/g, and (**F**) EIS curves of the samples.

Sample	Power density (W/Kg)	Energy density (Wh/Kg)
MoS_2	229.73	9.77
$MnFe_2O_4$	224.23	17.43
$MnFe_2O_4/MoS_2$	213.64	46.51

Table 2. The calculated energy densities and power densities of the samples at the current density of 1 A/g.

occupy the tetrahedral sites and octahedral sites, respectively, and Mn^{2+} and Fe^{3+} ions are distributed in the remaining tetrahedral and octahedral sites. Recently, we compared the experimental and theoretical results of $MnFe_2O_4$ and showed that the true XRD pattern of $MnFe_2O_4$ is a combination of normal and inverse spinel XRD patterns[14]. However, for the sake of simplicity, we considered here the normal spinel configuration for $MnFe_2O_4$ (see Fig. 11B). We considered a 28-atom unit cell for the bulk $MnFe_2O_4$ as half of a simple cubic structure. Figure 11B shows the unit cell and the atom-projected density of states of the bulk $MnFe_2O_4$. It is seen that the structure is an insulator with a direct bandgap of 1.41 eV. The *a* and *c* lattice constants were found 6.14 and 8.68 Å, respectively.

Next, we created the $MnFe_2O_4/MoS_2$ interface (see Fig. 11C). The lattice mismatch between the $MnFe_2O_4$ surface and the MoS_2 monolayer was ~ 5%. We applied the strain to the MoS_2 monolayer because it only affects its bandgap and cannot change its semiconducting nature[55]. In the optimized structure, the smallest distance between Mn and S atoms is 2.79 Å, which is larger than the sum of the covalent radii of both atoms (1.39 and 1.02 Å for Mn and S, respectively), indicating that the coupling between the $MnFe_2O_4$ slab and the MoS_2 monolayer is of the vdW type, not covalent. The binding energy between the MoS_2 monolayer and the $MnFe_2O_4$ slab is defined as:

$$E_b = E_{interface} - E_{MnFe_2O_4} - E_{MoS_2} \tag{7}$$

where E_b is the binding energy and $E_{MnFe_2O_4}$, E_{MoS_2}, and $E_{interface}$ are the total energies of the $MnFe_2O_4/MoS_2$ interface, the MoS_2 monolayer, and the $MnFe_2O_4$ slab, respectively. The binding energy (E_b) was calculated -1.44 eV per unit cell, indicating the physisorption nature of the coupling between the $MnFe_2O_4$ slab and the MoS_2 monolayer. The interlayer distance of 3.19 Å confirms again the vdW nature of the coupling between the individual layers. This indicates that the MoS_2 monolayer would not have any significant influence on the electronic properties of $MnFe_2O_4$ and just creates some energy levels near its Fermi level and redistributes the charge density of $MnFe_2O_4$ at its surface.

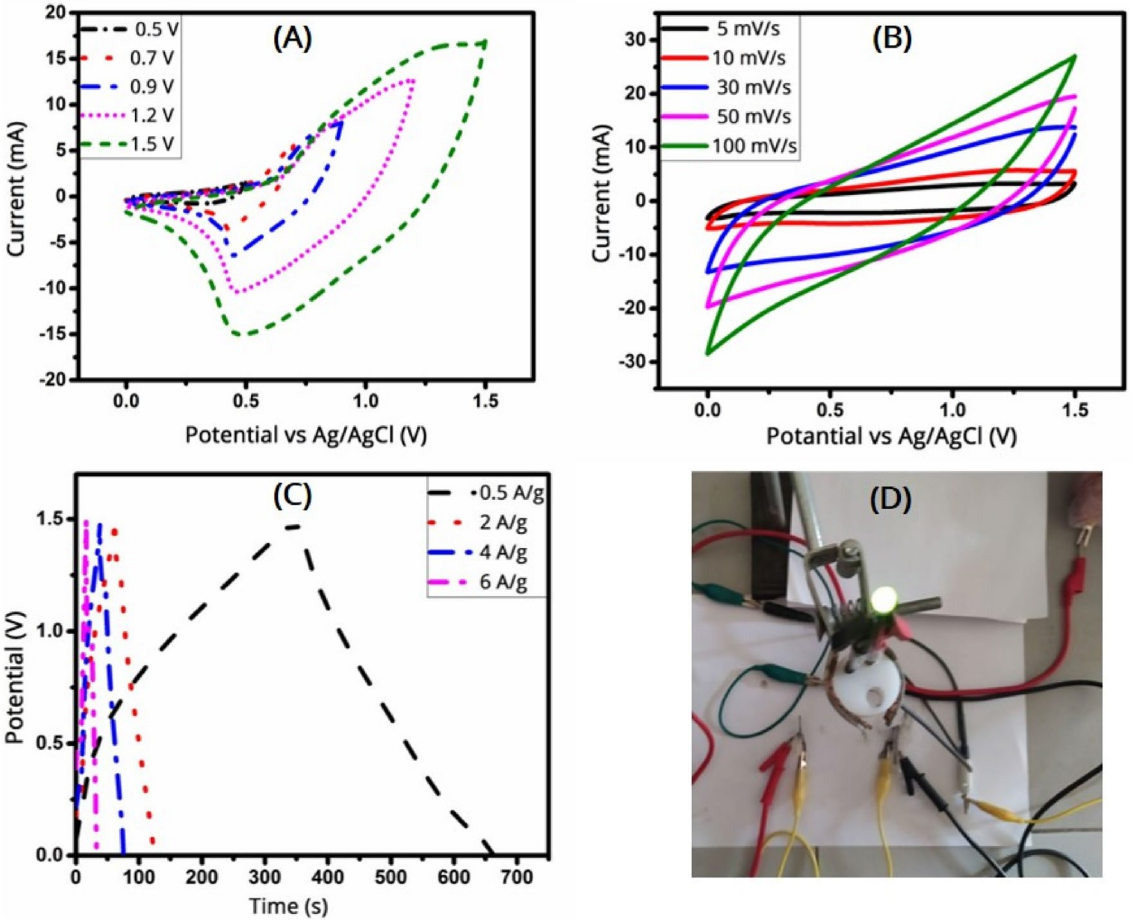

Figure 10. CV curves of the ($MnFe_2O_4$/MoS_2)//AC asymmetric supercapacitor (**A**) for different potential windows at 20 mV/s and (**B**) for different scan rates at the potential window of 1.5 V. (**C**) GCD curves of the supercapacitor at different current densities at the potential window of 1.5 V. (**D**) A picture of the assembled asymmetric supercapacitor lighting up a green LED.

Figure 12A shows the differential charge density of the $MnFe_2O_4$/MoS_2 interface (i.e., the charge density of the $MnFe_2O_4$/MoS_2 interface minus those of the isolated $MnFe_2O_4$ slab and the isolated MoS_2 monolayer). It is seen that the electrons just below the $MnFe_2O_4$ surface have been depleted, while they have been accumulated on the MoS_2 surface, more on the nearest sulfur layer, which is due to the higher electron affinity of S as compared to Mo. The integrated charge density difference was calculated using the following equation:

$$\Delta\rho(z) = \int \rho_{interface} dxdy - \int \rho_{MnFe_2O_4} dxdy - \int \rho_{MoS_2} dxdy \quad (8)$$

where $\rho_{interface}$, $\rho_{MnFe_2O_4}$, and ρ_{MoS_2} denote the charge densities corresponding to the $MnFe_2O_4$/MoS_2 interface, the $MnFe_2O_4$ slab, and the MoS_2 monolayer. The result is shown in Fig. 12B. The net charge transfer from the $MnFe_2O_4$ slab to the MoS_2 monolayer was calculated as 2 electrons. Figure 12C shows the in-plane averaged electrostatic potential of the $MnFe_2O_4$/MoS_2 interface along the z-direction. It is seen that the interface develops a very large difference (16.53 eV) in the in-plane averaged electrostatic potential across the interface, leading to a large intrinsic built-in electric field (E_{in}) from MoS_2 to $MnFe_2O_4$. This large built-in electric field drives electrons from $MnFe_2O_4$ towards MoS_2, enhancing the interlayer coupling. The attraction of charge density from $MnFe_2O_4$ to MoS_2 would help to enhance the charge storage of the composite. When charging, due to the constant transfer of electrons from the electrolyte to $MnFe_2O_4$ and in turn to MoS_2, a longer time would be needed to reach the charge saturation state (as seen in GCD curves in Fig. 9). When discharging, the process is reversed and a long time would be needed for a fully discharged state (again consistent with GCD curves in Fig. 9). This can enhance the specific capacitance of the pure $MnFe_2O_4$.

To sum up, according to the hybrid experimental and computational work, one can conclude that MoS_2 can enhance the charge storage capability and the specific capacitance of $MnFe_2O_4$ for several reasons: (1) MoS_2 itself can exhibit a supercapacitance behavior, (2) MoS_2 nanosheets will act as a substrate to hold $MnFe_2O_4$ nanoparticles uniformly so that they will not be agglomerated, (3) in a similar manner, the $MnFe_2O_4$ nanoparticles can prevent the MoS_2 nanosheets from restacking, (4) MoS_2 nanosheets provide a significantly higher active surface area, (5) MoS_2 would create several energy levels near the Fermi energy of $MnFe_2O_4$ that are suitable for charge

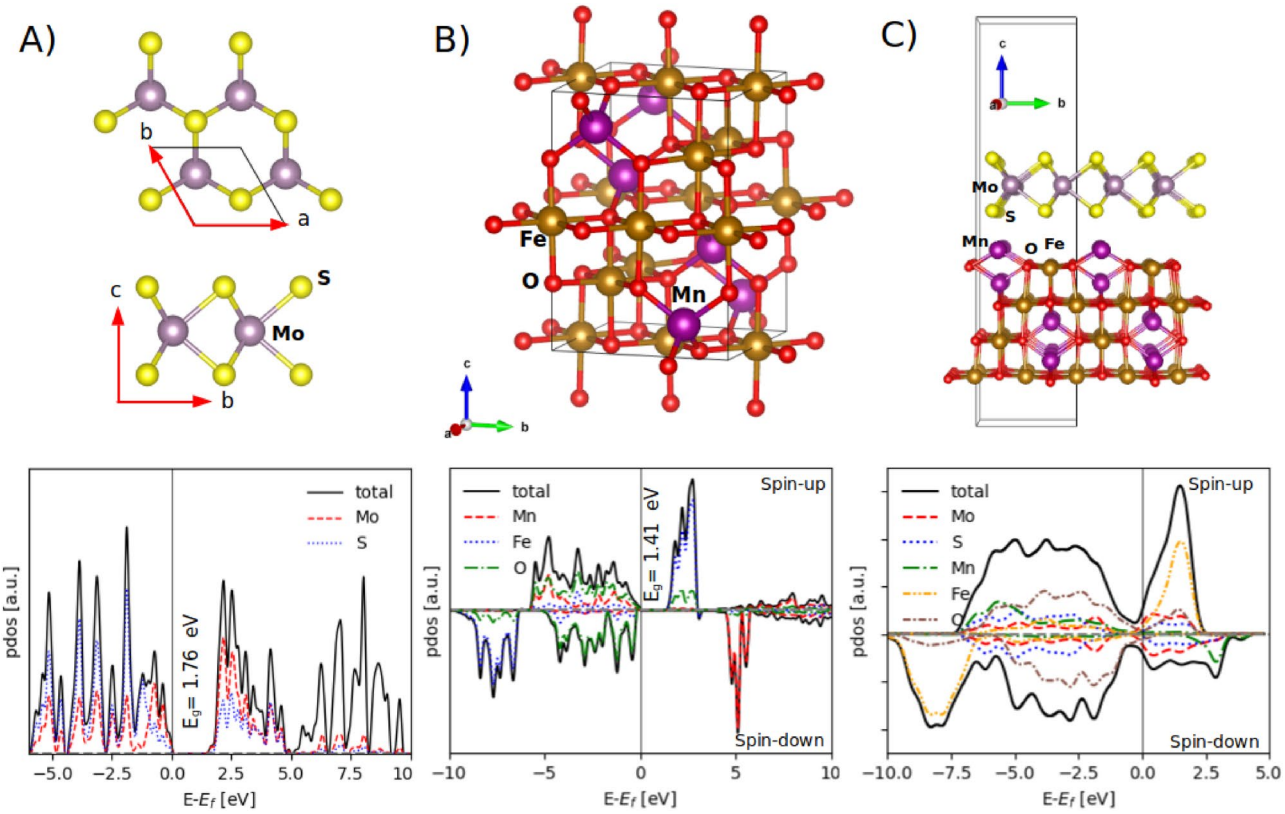

Figure 11. The unit cells and the atom-projected density of states of (**A**) the MoS_2 monolayer, (**B**) the normal spinel $MnFe_2O_4$, and (**C**) the $MnFe_2O_4/MoS_2$ interface. The crystal structure images were produced by VESTA (version 3.4.5)[39].

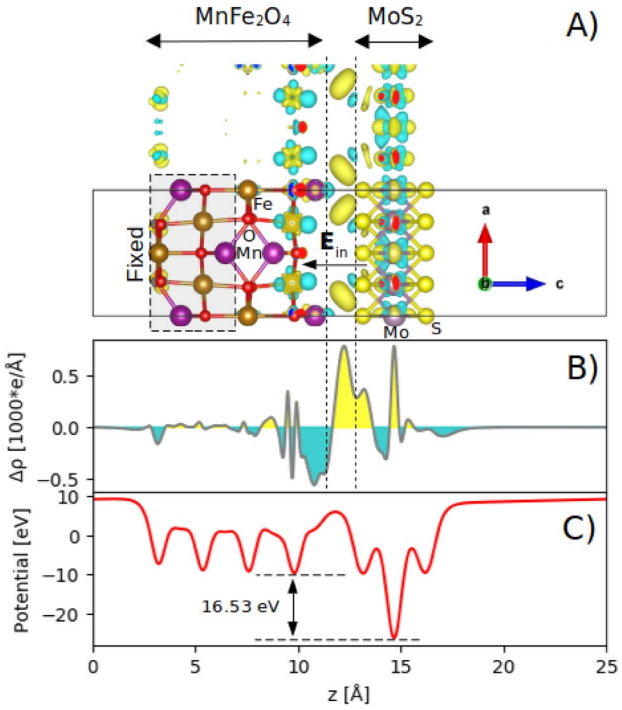

Figure 12. (Color online) (**A**) A 3D picture of the differential charge density of the $MnFe_2O_4/MoS_2$ interface, where the yellow and blue areas denote the gain and the loss of electrons, respectively, with the isosurface value of 0.016 e/Å^3, with (**B**) its corresponding in-plane averaged differential charge density along the z-direction. The space between the dashed lines contains no atom. (**C**) The in-plane averaged electrostatic potential of the $MnFe_2O_4/MoS_2$ interface.

storage, and (6) MoS_2 will attract the electron charge density from $MnFe_2O_4$ and constantly redistribute the stored charges. These all can synergistically enhance the specific capacitance of pure $MnFe_2O_4$ nanoparticles.

Conclusions

$MnFe_2O_4$ nanoparticles were in-situ synthesized on pre-exfoliated few-layer MoS_2 nanosheets via a simple hydrothermal method, and the synthesized $MnFe_2O_4/MoS_2$ nanocomposite was studied for supercapacitor applications. We found that owing to the effect of MoS_2, the $MnFe_2O_4/MoS_2$ nanocomposite demonstrates a considerably higher (~ 3.5 times) specific capacitance and better charge–discharge cycling stability as compared to pure $MnFe_2O_4$. Using DFT calculations, we attributed the improvement to the energy levels of MoS_2 near the Fermi level of the composite, making it a conductor, and the attraction of electron charge density from $MnFe_2O_4$ to MoS_2, which will help the redistribution of electrons between MoS_2 and $MnFe_2O_4$ when charging and discharging. Figure S1 (in the supplementary material) provides a summary schematic of the research findings.

Data availability

The datasets generated during and/or analyzed during the current study are available from the corresponding author on reasonable requests.

Received: 19 December 2020; Accepted: 5 April 2021
Published online: 16 April 2021

References

1. Chen, T.-Y. & Lin, L.-Y. Morphology variation for the nickel cobalt molybdenum copper oxide with different metal ratios and their application on energy storage. *Electrochim. Acta* **298**, 745–755 (2019).
2. Huang, Y.-Y. & Lin, L.-Y. Synthesis of ternary metal oxides for battery-supercapacitor hybrid devices: Influences of metal species on redox reaction and electrical conductivity. *ACS Appl. Energy Mater.* **1**, 2979–2990 (2018).
3. Liu, C., Neale, Z. G. & Cao, G. Understanding electrochemical potentials of cathode materials in rechargeable batteries. *Mater. Today* **19**, 109–123 (2016).
4. Rahimi, K. Electric-field- and strain-induced adjustability of vdW heterostructure of g-ZnO/2H-TiS2 for optoelectronic applications. *Mater. Lett.* **282**, 128680 (2021).
5. Rahimi, K. Tunable electronic properties of the novel g-ZnO/1T-TiS2 vdW heterostructure by electric field and strain: Crossovers in bandgap and band alignment types. *Phys. Chem. Chem. Phys.* **22**, 7412–7420 (2020).
6. Rahimi, K. & Yazdani, A. Incremental photocatalytic reduction of graphene oxide on vertical ZnO nanorods for ultraviolet sensing. *Mater. Lett.* **262**, 127078 (2020).
7. Khan, K. *et al.* Recent developments in emerging two-dimensional materials and their applications. *J. Mater. Chem. C* **8**, 387–440 (2020).
8. Kumar, P. *et al.* Review—two-dimensional layered materials for energy storage applications. *ECS J. Solid State Sci. Technol.* **5**, Q3021–Q3025 (2016).
9. Rahimi, K., Moradi, M., Dehghan, R. & Yazdani, A. Enhancement of sunlight-induced photocatalytic activity of ZnO nanorods by few-layer MoS2 nanosheets. *Mater. Lett.* **234**, 134–137 (2019).
10. Lin, L. *et al.* Two-dimensional transition metal dichalcogenides in supercapacitors and secondary batteries. *Energy Storage Mater.* **19**, 408–423 (2019).
11. Chia, X., Ambrosi, A., Lazar, P., Sofer, Z. & Pumera, M. Electrocatalysis of layered Group 5 metallic transition metal dichalcogenides (MX2, M = V, Nb, and Ta; X = S, Se, and Te). *J. Mater. Chem. A* **4**, 14241–14253 (2016).
12. Pumera, M., Sofer, Z. & Ambrosi, A. Layered transition metal dichalcogenides for electrochemical energy generation and storage. *J. Mater. Chem. A* **2**, 8981–8987 (2014).
13. Shi, L. & Zhao, T. Recent advances in inorganic 2D materials and their applications in lithium and sodium batteries. *J. Mater. Chem. A* **5**, 3735–3758 (2017).
14. Sharifi, S., Yazdani, A. & Rahimi, K. Incremental substitution of Ni with Mn in NiFe2O4 to largely enhance its supercapacitance properties. *Sci. Rep.* **10**, 2 (2020).
15. Sharifi, S., Yazdani, A. & Rahimi, K. Effect of Co2 content on supercapacitance properties of hydrothermally synthesized Ni1-xCoxFe2O4 nanoparticles. *Mater. Sci. Semicond. Process.* **108**, 104902 (2020).
16. Fu, W., Xu, X., Wang, W., Shen, J. & Ye, M. In-situ growth of NiFe2O4/2D MoS2 p-n heterojunction immobilizing palladium nanoparticles for enhanced visible-light photocatalytic activities. *ACS Sustain. Chem. Eng.* **6**, 8935–8944 (2018).
17. Kubakaddi, S. S. Large power dissipation of hot Dirac fermions in twisted bilayer graphene. *J. Phys. Condens. Matter* https://doi.org/10.1088/1361-648X/abd526 (2020).
18. Moosavifard, S. E., Najafi, F., Izadi, M., Gharibzadeh, Z. & Habibi, Z. Facile synthesis of nanoporous spinel nickel-manganese-cobalt ternary oxide hollow spheres as high-performance supercapacitor electrode material. *Adv. Nanochem.* **2**, 7–10 (2020).
19. Zeng, D. *et al.* Enhanced hydrogen production performance through controllable redox exsolution within CoFeAlOx spinel oxygen carrier materials. *J. Mater. Chem. A* **6**, 11306–11316 (2018).
20. Yan, Y. *et al.* Bifunctional nickel ferrite-decorated carbon nanotube arrays as free-standing air electrode for rechargeable Zn–air batteries. *J. Mater. Chem. A* **8**, 5070–5077 (2020).
21. Su, L. *et al.* Sprinkling MnFe2O4quantum dots on nitrogen-doped graphene sheets: The formation mechanism and application for high-performance supercapacitor electrodes. *J. Mater. Chem. A* **6**, 9997–10007 (2018).
22. Zhang, Z. *et al.* Layer-stacked cobalt ferrite (CoFe2O4) mesoporous platelets for high-performance lithium ion battery anodes. *J. Mater. Chem. A* **3**, 6990–6997 (2015).
23. Yazdani, A., Zafarkish, H. & Rahimi, K. The variation of Eg-shape dependence of NiO nanoparticles by the variation of annealing temperature. *Mater. Sci. Semicond. Process.* **74**, 225–231 (2018).
24. Rahimi, K., Zafarkish, H. & Yazdani, A. Reduced graphene oxide can activate the sunlight-induced photocatalytic effect of NiO nanowires. *Mater. Des.* **144**, 214–221 (2018).
25. Mohammadi, A., Moosavifard, S. E., Tabrizi, A. G., Abdi, M. M. & Karimi, G. Nanoporous CuCo2S4 microspheres: A novel positive electrode for high-performance hybrid energy storage devices. *ACS Appl. Energy Mater.* **2**, 627–635 (2019).
26. Pan, J. *et al.* The NiFe2O4/NiCo2O4/GO composites electrode material derived from dual-MOF for high performance solid-state hybrid supercapacitors. *Colloids Surf., A* **609**, 125650 (2021).
27. Tomboc, G. M. *et al.* Hybrid layered double hydroxides as multifunctional nanomaterials for overall water splitting and supercapacitor applications. *J. Mater. Chem. A Mater. Energy Sustain.* https://doi.org/10.1039/D0TA11606H (2021).
28. Zhou, R. *et al.* Charge storage by electrochemical reaction of water bilayers absorbed on MoS monolayers. *Sci. Rep.* **9**, 3980 (2019).

29. Feng, N. *et al.* A polymer-direct-intercalation strategy for MoS/carbon-derived heteroaerogels with ultrahigh pseudocapacitance. *Nat. Commun.* **10**, 1372 (2019).
30. Wang, G. *et al.* Controlled synthesis of CoFe2O4/MoS2 nanocomposites with excellent sedimentation stability for magnetorheological fluid. *J. Ind. Eng. Chem.* **70**, 439–446 (2019).
31. Zeng, Y. *et al.* Fabrication of Z-scheme magnetic MoS2/CoFe2O4 nanocomposites with highly efficient photocatalytic activity. *J. Colloid Interface Sci.* **514**, 664–674 (2018).
32. Zhao, Y. *et al.* Facile preparation of NiFe2O4/MoS2 composite material with synergistic effect for high performance supercapacitor. *J. Alloy. Compd.* **726**, 608–617 (2017).
33. Dong, L. *et al.* Spontaneous exfoliation and tailoring of MoS2 in mixed solvents. *Chem. Commun.* **50**, 15936–15939 (2014).
34. Gogotsi, Y. & Penner, R. M. Energy storage in nanomaterials—capacitive, pseudocapacitive, or battery-like?. *ACS Nano* **12**, 2081–2083 (2018).
35. Giannozzi, P. *et al.* QUANTUM ESPRESSO: A modular and open-source software project for quantum simulations of materials. *J. Phys. Condens. Matter* **21**, 395502 (2009).
36. Vanderbilt, D. Soft self-consistent pseudopotentials in a generalized eigenvalue formalism. *Phys. Rev. B* **41**, 7892–7895 (1990).
37. Perdew, J. P., Burke, K. & Ernzerhof, M. Generalized Gradient Approximation Made Simple [Phys. Rev. Lett. 77, 3865 (1996)]. *Phys. Rev. Lett.* **78**, 1396–1396 (1997).
38. Cococcioni, M. & de Gironcoli, S. Linear response approach to the calculation of the effective interaction parameters in theLDA Umethod. *Phys. Rev. B* **71**, 2 (2005).
39. Momma, K. & Izumi, F. VESTA 3for three-dimensional visualization of crystal, volumetric and morphology data. *J. Appl. Crystallogr.* **44**, 1272–1276 (2011).
40. Prabhu, Y. T., Rao, K. V., Kumar, V. S. S. & Kumari, B. S. X-ray analysis by williamson-hall and size-strain plot methods of ZnO nanoparticles with fuel variation. *World J. Nano Sci. Eng.* **04**, 21–28 (2014).
41. Hussein, H. & Yazdani, A. Investigation the influence of Fe (III) doping in Cu2ZnSnS4 semiconductor: Structural, optical and magnetic properties. *Optik* **179**, 505–513 (2019).
42. Li, H. *et al.* From bulk to monolayer MoS2: Evolution of Raman scattering. *Adv. Func. Mater.* **22**, 1385–1390 (2012).
43. Ulpe, A. C. *et al.* Photoelectrochemistry of ferrites: Theoretical predictions vs experimental results. *Z. Phys. Chem.* **234**, 719–776 (2020).
44. Devine, T. M. & Adar, F. Raman Spectroscopy of Solids. in *Characterization of Materials* (ed. Kaufmann, E. N.) (2012). doi:https://doi.org/10.1002/0471266965.com060.pub2.
45. Ren, B., Shen, W., Li, L., Wu, S. & Wang, W. 3D CoFe2O4 nanorod/flower-like MoS2 nanosheet heterojunctions as recyclable visible light-driven photocatalysts for the degradation of organic dyes. *Appl. Surf. Sci.* **447**, 711–723 (2018).
46. Pak, M., Moshaii, A., Siampour, H., Abbasian, S. & Nikkhah, M. Cobalt-copper bimetallic nanostructures prepared by glancing angle deposition for non-enzymatic voltammetric determination of glucose. *Mikrochim. Acta* **187**, 276 (2020).
47. Eskandari, M., Malekfar, R., Buceta, D. & Taboada, P. NiCo2O4-based nanostructured composites for high-performance pseudocapacitor electrodes. *Colloids Surf., A* **584**, 124039 (2020).
48. Bhujun, B., Tan, M. T. T. & Shanmugam, A. S. Study of mixed ternary transition metal ferrites as potential electrodes for supercapacitor applications. *Results Phys.* **7**, 345–353 (2017).
49. Wang, H. *et al.* Preparation and performance of PANI/RFC/rGO composite electrode materials for supercapacitors. *Ionics* **26**, 4031–4038 (2020).
50. Jeyaranjan, A., Sakthivel, T. S., Neal, C. J. & Seal, S. Scalable ternary hierarchical microspheres composed of PANI/ rGO/CeO2 for high performance supercapacitor applications. *Carbon* **151**, 192–202 (2019).
51. Huang, K.-J. *et al.* Layered MoS2–graphene composites for supercapacitor applications with enhanced capacitive performance. *Int. J. Hydrogen Energy* **38**, 14027–14034 (2013).
52. Kobayashi, K. & Yamauchi, J. Electronic structure and scanning-tunneling-microscopy image of molybdenum dichalcogenide surfaces. *Phys. Rev. B Condens. Matter* **51**, 17085–17095 (1995).
53. Yun, W. S., Han, S. W., Hong, S. C., Kim, I. G. & Lee, J. D. Thickness and strain effects on electronic structures of transition metal dichalcogenides: 2H-MX2semiconductors (M=Mo, W;X=S, Se, Te). *Phys. Rev. B* **85**, 2 (2012).
54. Szotek, Z. *et al.* Electronic structures of normal and inverse spinel ferrites from first principles. *Phys. Rev. B* **74**, 2 (2006).
55. Lu, P., Wu, X., Guo, W. & Zeng, X. C. Strain-dependent electronic and magnetic properties of MoS2 monolayer, bilayer, nanoribbons and nanotubes. *Phys. Chem. Chem. Phys.* **14**, 13035 (2012).

Acknowledgements

The authors would like to thank the Research Council of Tarbiat Modares University for financial support.

Author contributions

S.S. and K.R. equivalently contribute to the manuscript. K.R. performed DFT simulations. A.Y. supervised the project.

Competing interests

The authors declare no competing interests.

Additional information

Supplementary Information The online version contains supplementary material available at https://doi.org/10.1038/s41598-021-87823-6.

Correspondence and requests for materials should be addressed to A.Y.

Reprints and permissions information is available at www.nature.com/reprints.

Publisher's note Springer Nature remains neutral with regard to jurisdictional claims in published maps and institutional affiliations.